



| | |
|----------------------------------|--|
| Publication Year | 2022 |
| Acceptance in OA | 2022-10-03T15:06:27Z |
| Title | Galaxies in the central regions of simulated galaxy clusters |
| Authors | RAGAGNIN, ANTONIO, MENEGHETTI, MASSIMO, BASSINI, LUIGI, Ragone-Figueroa, Cinthia, GRANATO, Gian Luigi, Despali, Giulia, GIOCOLI, Carlo, GRANATA, Giovanni, MOSCARDINI, LAURO, BERGAMINI, PIETRO, RASIA, ELENA, VALENTINI, MILENA, BORGANI, Stefano, CALURA, Francesco, Dolag, Klaus, GRILLO, CLAUDIO, MERCURIO, AMATA, MURANTE, Giuseppe, Natarajan, Priyamvada, Rosati, Piero, TAFFONI, Giuliano, TORNATORE, Luca, Tortorelli, Luca |
| Publisher's version (DOI) | 10.1051/0004-6361/202243651 |
| Handle | http://hdl.handle.net/20.500.12386/32680 |
| Journal | ASTRONOMY & ASTROPHYSICS |
| Volume | 665 |

Galaxies in the central regions of simulated galaxy clusters

Antonio Ragagnin^{1,2,3} , Massimo Meneghetti^{4,5}, Luigi Bassini⁶, Cinthia Ragone-Figueroa^{7,2}, Gian Luigi Granato^{2,7,3}, Giulia Despali⁸, Carlo Giocoli^{4,5,1}, Giovanni Granata⁹, Lauro Moscardini^{1,4,5}, Pietro Bergamini^{9,4}, Elena Rasia^{2,3}, Milena Valentini¹⁰, Stefano Borgani^{11,2}, Francesco Calura⁴, Klaus Dolag^{10,12}, Claudio Grillo^{9,13}, Amata Mercurio¹⁴, Giuseppe Murante^{2,3}, Priyamvada Natarajan¹⁵, Piero Rosati^{13,16}, Giuliano Taffoni², Luca Tornatore², and Luca Tortorelli¹⁰

(Affiliations can be found after the references)

Received 27 March 2022 / Accepted 14 June 2022

ABSTRACT

Context. Recent observations found that observed cluster member galaxies are more compact than their counterparts in Λ CDM hydrodynamic simulations, as indicated by the difference in their strong gravitational lensing properties, and they reported that measured and simulated galaxy–galaxy strong lensing events on small scales are discrepant by one order of magnitude. Among the possible explanations for this discrepancy, some studies suggest that simulations with better resolution and implementing different schemes for galaxy formation could produce simulations that are in better agreement with the observations.

Aims. In this work, we aim to assess the impact of numerical resolution and of the implementation of energy input from AGN feedback models on the inner structure of cluster sub-haloes in hydrodynamic simulations.

Methods. We compared several zoom-in re-simulations of a sub-sample of cluster-sized haloes obtained by varying mass resolution and softening the length and AGN energy feedback scheme. We studied the impact of these different setups on the sub-halo (SH) abundances, their radial distribution, their density and mass profiles, and the relation between the maximum circular velocity, which is a proxy for SH compactness

Results. Regardless of the adopted numerical resolution and feedback model, SHs with masses of $M_{\text{SH}} \lesssim 10^{11} h^{-1} M_{\odot}$, the most relevant mass range for galaxy–galaxy strong lensing, have maximum circular velocities $\sim 30\%$ smaller than those measured from strong lensing observations. We also find that simulations with less effective AGN energy feedback produce massive SHs ($M_{\text{SH}} \gtrsim 10^{11} h^{-1} M_{\odot}$) with higher maximum circular velocity and that their $V_{\text{max}}-M_{\text{SH}}$ relation approaches the observed one. However, the stellar-mass number count of these objects exceeds the one found in observations, and we find that the compactness of these simulated SHs is the result of an extremely over-efficient star formation in their cores, also leading to larger than observed SH stellar mass.

Conclusions. Regardless of the resolution and galaxy formation model adopted, simulations are unable to simultaneously reproduce the observed stellar masses and compactness (or maximum circular velocities) of cluster galaxies. Thus, the discrepancy between theory and observations that emerged previous works. It remains an open question as to whether such a discrepancy reflects limitations of the current implementation of galaxy formation models or the Λ CDM paradigm.

Key words. methods: numerical – galaxies: abundances – galaxies: clusters: general – galaxies: formation – Galaxy: evolution – galaxies: structure

1. Introduction

The properties and abundances of cluster sub-haloes (SHs) and their associated galaxies are important probes of cosmology (see e.g., Natarajan & Kneib 1997; Moore et al. 1998; Tormen et al. 1998; Natarajan & Springel 2004; Gao et al. 2004; van den Bosch et al. 2005; Kravtsov & Borgani 2012; Despali et al. 2016; Despali & Vegetti 2017; Natarajan et al. 2019; Ragagnin et al. 2021) and galaxy formation (Taylor & Kobayashi 2015). In particular, they can be used to test the predictions of the cold dark matter (CDM) paradigm of structure formation on multiple scales in clusters (see e.g., Natarajan et al. 2007; Yang & Yu 2021).

Gravitational lensing has proved to be a powerful tool to map the distribution of dark matter (DM) in galaxy clusters both on large and small scales (as in Grillo et al. 2015; Zitrin et al. 2015; Meneghetti et al. 2017; Kneib & Natarajan 2011; Umetsu 2020). In particular, recent improvements in combined strong plus weak lensing modelling techniques along with galaxy kinematic measurements from integral field spectroscopy, enabled us to constrain the matter distribution in cluster substructures in great detail (see e.g., Tremmel et al. 2019; Bergamini et al. 2019).

Based on cluster reconstructions, Meneghetti et al. (2020) (M20) recently reported that lensing clusters observed in the CLASH survey (Postman et al. 2012) and Frontier Fields (Lotz et al. 2017) HST programmes have cross-sections for galaxy–galaxy strong projected lensing (GGSL) that exceed the expectations in the context of current Λ CDM-based hydrodynamic simulations by one order of magnitude. The ability of sub-haloes to produce strong lensing events depends primarily on their compactness and location within the cluster. More compact SHs lying at smaller projected cluster-centric radii can more easily exceed the critical surface mass density required for strong lensing and can therefore be more effective at splitting and strongly distorting the images of background galaxies.

The spatial distribution of cluster SHs can be traced by the galaxies that they host. The maximum circular velocity is defined as

$$V_{\text{max}} = \max \left(\sqrt{\frac{GM(<r)}{r}} \right), \quad (1)$$

where r is the three-dimensional distance from the SH centre, $M(<r)$ is the SH radial mass profile, and G is the gravitational

constant. The value of V_{\max} has been demonstrated to be a robust proxy for SH compactness. As shown by Bergamini et al. (2019), the SH circular velocity can be measured by combining imaging and spectroscopic observations of strong lensing.

M20 noted that the galaxies with a projected distance within $\sim 0.15R_{\text{vir}}$ (where R_{vir} is the cluster virial radius¹) in the clusters reconstructed by Bergamini et al. (2019) have maximum circular velocities exceeding those of SHs with the same mass in the hydrodynamic simulations of Rasia et al. (2015, hereafter R15) by $\sim 30\text{--}50\%$ on average. They also found that the number density of these SHs near the cluster secondary critical lines in observations is higher than in simulations. Thus, M20 concluded that the larger GGSL cross-section reflects the more compact spatial distribution and internal structure of observed SHs compared to simulated ones.

This mismatch may arise due to limitations in our current simulations or may warrant revisiting our assumptions on the nature of dark matter (see e.g., Despali et al. 2020; Bhattacharyya et al. 2022; Yang & Yu 2021; Nguyen et al. 2021). Moreover, it has been argued that the simulation results might depend on mass resolution and artificial tidal disruption, which could impact the properties of SHs (Green et al. 2021). M20 performed a comparison between low- and high-resolution re-simulations of a single cluster and did not notice significant differences between their derived GGSL cross sections. Nevertheless, in a recent paper, Bahé (2021) claimed that cluster SHs in the very-high-resolution Hydrangea simulation suite are in better agreement with observations (see also Robertson 2021). We will devote part of this paper to assessing the origin of these two contradicting claims.

On top of this, most high-resolution hydrodynamic simulations have problems in reproducing correct stellar masses of high mass SHs. For instance, Ragone-Figueroa et al. (2018, RF18) showed that the stellar masses of the observed brightest cluster galaxies (BCGs) are clearly overproduced by the Hydrangea and IllustrisTNG simulations (see their Fig. 1). The excess of star formation in these simulations (i.e., the one shown in Fig. 3 in Genel et al. 2014, on the IllustrisTNG simulations) is likely related to a general difficulty in modelling AGN feedback at the high stellar mass regime. In other words, it seems that these simulations are not able to match observations of stellar masses (and therefore their baryon fractions), measured luminosities, internal structure, and lensing properties simultaneously.

It is important to note here that in addition to numerical resolution, the inner structure of SHs is very sensitive to the details of sub-grid models for cooling, star formation, and feedback implemented in the simulations. As M20 suggested, numerical effects may also play an important role in affecting the discrepancy they report. RF18 pointed out that particular care must be taken in controlling the centring of supermassive black hole (SMBH) particles, which leave their host galaxies in the course of the simulations due to frequent dynamical disturbances and mergers, the effects of which are probably amplified by numerical limitations. Under these circumstances, the SMBH energy feedback does not effectively suppress gas over-cooling (Borgani et al. 2006; Wurster & Thacker 2013) or star formation in the centre of massive galaxies (Ludlow et al. 2020; Bahé et al. 2022). Thus, it is worth studying the impact of feedback schemes, softening, and resolution in producing the $M_{\text{SH}}\text{--}V_{\max}$ relation.

¹ We denote the radius and mass of the sphere enclosing a density equal to Δ times the critical density at the respective redshift as R_{Δ} and M_{Δ} . See Naderi et al. (2015) for a review on galaxy cluster masses and radii definitions.

Moreover, when comparing density profiles of simulated haloes to observations, it is crucial to take into account that different softening lengths ϵ lead to varying minimum well-resolved radii, below which density profiles cannot be trusted as the gravitational force is underestimated². This minimum radius for density profiles is often estimated as 2.8 times the fiducial equivalent softening, that is $h \approx 2.8\epsilon$ (see Hernquist 1987 for more details on the choice of this value). For these reasons, in order to disentangle the effect of resolution alone, in this work we used simulations with varying softening, resolution, and feedback parameters in order to tackle all these small-scale issues.

The paper is organised as follows. In Sect. 2, we present our simulations in detail. In Sect. 3, we discuss the results in terms of mass–velocity SH scaling relations, and we present our conclusions and discussion thereof in Sect. 4.

2. Numerical setup

The Dianoga suite of simulations consists of a set of 29 regions containing cluster-size haloes extracted from a parent DM-only cosmological box of side-length 1 comoving h^{-1} Gpc. These regions were re-simulated including baryons, using the zoom-in initial conditions from Bonafede et al. (2011), and assuming different baryonic physics models, softening, and mass resolutions.

The simulations were performed using the code P-Gadget3 (Springel et al. 2001), adopting an improved smoothed particle hydrodynamics (SPH) solver (Beck et al. 2016) and a stellar evolution scheme (Tornatore et al. 2007; Springel et al. 2005b) that follows 11 chemical elements (H, He, C, N, O, Ne, Mg, Si, S, Ca, Fe) with the aid of the CLOUDY photo-ionisation code (Ferland et al. 1998). A general description of how the SMBH and energy feedback are modelled can be found in Springel et al. (2005b), Fabjan et al. (2010), Hirschmann et al. (2014), and Schaye et al. (2015).

2.1. Feedback schemes and resolutions

In this work, we focused on six Dianoga regions re-simulated with three models at low-resolution (1 \times), each model with different softening and feedback schemes. One of these models also has a high-resolution counterpart in order to isolate the effect of resolution alone (hereafter 10 \times B20 simulations, where ‘10 \times ’ means it has been re-simulated with a 10 times lower particle mass). The four suites are the following:

The 1 \times R15 model, described in R15 and in Planelles et al. (2017), uses the SMBH feedback scheme presented in Steinborn et al. (2015), and implements both mechanical and radiative feedback. The model is parameterised by an outflow efficiency ϵ_0 that regulates gas heating power P_0 used for mechanical feedback, while the radiative efficiency ϵ_r regulates the luminosity of the radiative component. The feedback energy per unit time in this model is then the sum of P_0 and the fraction ϵ_r of the luminosity (see Eqs. (7)–(12) in Steinborn et al. 2015 for more details). This model is an improvement on the model presented in Hirschmann et al. (2014), wherein a constant radiative efficiency is assumed that does not allow for a smooth transition between the quasar-mode and the radio-mode. In the model presented in Steinborn et al. (2015), the amount of energy released by SMBH growth is determined by the radiative

² For two particles with distance r , their gravitational potential is computed as $\Phi \propto 1/\sqrt{r^2 + \epsilon^2}$.

efficiency factor ϵ_r and the fraction that is thermally coupled with the surrounding gas is denoted by ϵ_f . These simulations have been used in M20 in order to compare simulations with observational data. R15 showed that their model produces cool-core clusters in similar proportions to observations from Eckert et al. (2011).

The $1 \times \text{RF18}$ model is described in Ragone-Figueroa et al. (2013) with some modifications introduced in RF18. At variance with Springel et al. (2005a), Ragone-Figueroa et al. (2013) implemented a mechanism of cold-cloud evaporation, so that if gas in the cold phase is heated by the AGN energy to a temperature that exceeds the average gas temperature, then the corresponding particle is removed from the multi-phase state to avoid star formation. To prevent the particle from re-entering the multi-phase state in the next time step, they added a maximum temperature condition for a particle to be star-forming (as explained in Sect. 2.1 of Ragone-Figueroa et al. 2013). These simulations have a larger softening compared to $1 \times \text{R15}$. The simulated BCG mass evolution and the BCG alignment with the host cluster are in agreement with observational data (Ragone-Figueroa et al. 2018, 2020).

The $10 \times \text{B20}$ model is presented in Bassini et al. (2020) (B20), where the regions are re-simulated with a mass resolution 10 times higher than the above-mentioned $1 \times$ models. They have a feedback scheme similar to $1 \times \text{RF18}$; however, they do not implement cold cloud evaporation in order to reduce the feedback efficiency. As a consequence, the sample reproduces the stellar mass function (SMF) from Bernardi et al. (2013) over more than one order of magnitude in the intermediate SH mass regime; however, it overproduces the number count of most massive galaxies. We also created the $1 \times \text{B20}$ sample to isolate the effect of resolution on SHs. We re-simulated four regions with the same feedback configuration of B20 $10 \times \text{B20}$ and re-scaled their softening parameters to the $1 \times$ resolution level.

In Table 1, we report all feedback parameters, softening, and mass resolution values for the four suites $1 \times \text{R15}$, $1 \times \text{RF18}$, $10 \times \text{B20}$, and $1 \times \text{B20}$. There, we report the minimum gas temperature allowed for cooling, $\min T_g$, an outflow efficiency ϵ_o , the BH radiative efficiency ϵ_r , and the feedback efficiency ϵ_f (see Shakura & Sunyaev 1973; Steinborn et al. 2015, for more details). These parameters have been tuned to fit some observational properties of galaxy clusters best:

R15 and B20 tuned the stellar mass vs. black hole (BH) mass relation $M_\star - M_{\text{BH}}$, i.e., the Magorrian relation (Magorrian et al. 1998), and the stellar mass function (in the case of $10 \times$), while RF18 tuned the Magorrian and the BCG mass vs. M_{500c} relation.

We note that even if some re-simulations have similar feedback parameter values, they have different feedback implementations (see discussion in Sects. 2 and 3 of B20). In particular, the RF18 scheme takes into account cold cloud evaporation (see the appendix in Ragone-Figueroa et al. 2013) and uses a multi-phase particle criterion depending not only on density but also on temperature. On the other hand, the B20 scheme removes the temperature criterion. Thus, the high-density particles cool more efficiently (see appendix in Ragone-Figueroa et al. 2013). As a result, the B20 scheme leads to a better agreement of SMF with observations and has less efficient feedback than $1 \times \text{RF18}$. Unlike the other three setups, the $1 \times \text{B20}$ realisation has not been tuned with respect to any observational data.

2.2. Zoom-in regions

Firstly, in the following analyses, we focused primarily on SHs with $M_{\text{SH}} > 2 \times 10^{10} h^{-1} M_\odot$, whose inner structure is resolved

Table 1. List of feedback and resolution parameters for the four suites $1 \times \text{R15}$, $1 \times \text{RF18}$, $10 \times \text{B20}$, and its $1 \times$ counterpart ($1 \times \text{B20}$).

| | $1 \times \text{R15}$ | $1 \times \text{RF18}$ | $10 \times \text{B20}$ | $1 \times \text{B20}$ |
|---|-----------------------|------------------------|------------------------|-----------------------|
| $\min T_g [\text{K}]$ | 50 | 50 | | 20 |
| ϵ_o | 0.15 | – | | – |
| ϵ_r | 0.1 | 0.07 | | 0.07 |
| ϵ_f | 0.05 | 0.1 | | 0.16 |
| $\epsilon_{\text{DM}} [h^{-1} \text{akpc}]$ | 3.75 | 5.62 | 1.4 | 3.0 |
| $\epsilon_\star [h^{-1} \text{akpc}]$ | 2.0 | 3.0 | 0.35 | 0.75 |
| $m_{\text{DM}} [10^8 h^{-1} M_\odot]$ | 8.3 | 8.3 | 0.83 | 8.3 |
| Reference | R15 | RF18 | | B20 |

Notes. Rows show, respectively, minimum gas temperature T_g , outflow efficiency ϵ_o , BH radiative efficiency ϵ_r , BH feedback factor ϵ_f , dark-matter softening ϵ_{DM} , stellar softening ϵ_\star , and dark-matter particle mass m_{DM} .

Table 2. Cluster haloes studied in this work.

| Name | $1 \times \text{R15}$ | | $1 \times \text{RF18}$ | | $10 \times \text{B20}$ | | $1 \times \text{B20}$ | |
|------|-----------------------|-------|------------------------|-------|------------------------|-------|-----------------------|-------|
| | M_{vir} | N_s | M_{vir} | N_s | M_{vir} | N_s | M_{vir} | N_s |
| D1 | 11.4 | 62 | 11.4 | 38 | 11.1 | 87 | | |
| D3 | 4.9 | 25 | 4.8 | 13 | 4.8 | 28 | 4.8 | 21 |
| D6 | 6.3 | 28 | 6.3 | 25 | 6.4 | 42 | 6.4 | 34 |
| D10 | 10.4 | 70 | 10.4 | 48 | 10.1 | 83 | | |
| D18 | 8.0 | 32 | 8.1 | 23 | 7.7 | 49 | 7.6 | 31 |
| D25 | 3.1 | 13 | 3.0 | 12 | 3.0 | 22 | 2.3 | 13 |

Notes. First column reports the names of the 6 out of the 29 Dianoga regions used in this work. The panels in other columns are the halo virial masses (M_{vir}) and the number N_s of SHs with mass $M_{\text{SH}} > 2 \times 10^{10} h^{-1} M_\odot$ within a distance of $r < 0.15 R_{\text{vir}}$ from the halo centre. These quantities are reported for all suites ($1 \times \text{R15}$, $1 \times \text{RF18}$, $10 \times$, and $1 \times \text{B20}$). Virial masses are in units of $10^{14} h^{-1} M_\odot$. Haloes are extracted at redshift $z = 0.4$.

with ≥ 100 particles. In each region we focus on the main central halo at $z = 0.4$, in order to consistently compare the redshift of observations presented in Bergamini et al. (2019) and Granata et al. (2022). We considered three lines of sight orthogonal to each cluster halo and extracted all SHs in cylinders with depths of 10 comoving $h^{-1} \text{Mpc}$ and radii of $R < 0.15 R_{\text{vir}}$ centred on the halo centre. This radius is roughly consistent with that of the region that typically contains the cluster secondary critical lines for strong lensing (see e.g., M20).

In Table 2, we present properties of the six regions (D1, D3, D6, D10, D18, D25) used in this work, all with a virial mass of $M_{\text{vir}} > 3 \times 10^{14} h^{-1} M_\odot$. All regions that have been re-simulated assume a ΛCDM cosmology with the parameters $\Omega_m = 0.24$, $\Omega_b = 0.04$, $n_s = 0.96$, $\sigma_8 = 0.8$, and $h = 0.72$.

Table 2 shows virial masses and the number (averaged over the three different projections) of SHs of the six regions in the four suites. From the table it is already possible to appreciate a difference in the amount of SHs identified in different simulations, with smaller softening and particle mass values generally leading to the formation of a larger number of SHs.

2.3. SH selection methods

The haloes and SHs are identified using the friend-of-friend halo finder (Davis et al. 1985; Springel 2005) and an improved

version of the SH finder SUBFIND (Springel et al. 2001), respectively. The latter takes into account the presence of baryons (Dolag et al. 2009). For each region in which we identify the most massive FoF halo and its centre of mass, SH particles are found by SUBFIND, which iteratively removes unbound particles within the contour that traverses the gravitational potential saddle points (see Muldrew et al. 2011 for more information on its accuracy).

In this work, we considered stellar masses hosted in SHs as the sum of all bounded star particles within 50 and 30 physical projected kpc. This aperture is chosen as the ones in the observations of Kravtsov et al. (2018) and Bergamini et al. (2019), respectively.

3. Results

3.1. SH masses

The top panel of Fig. 1 shows the BCG stellar masses against the total mass within R_{500c} of our four suites and observations from Kravtsov et al. (2018). Here, we can see that $1 \times R15$ and $1 \times RF18$ have BCGs that tend to agree with observations, while B20s $1 \times$ and $10 \times$ simulations have BCGs much brighter than observations, as expected with their low feedback.

We now show that the overproduction of stars is not limited to BCGs. The total stellar mass within R_{500c} (i.e., $M_{\star,500c}$, presented in second panel of Fig. 1) is systematically higher than observations for both B20 models, while RF18 and R15 produce a lower number of stars, which is closer to the observed values.

In the third panel of Fig. 1, where we compare the stellar mass in satellites as estimated by Kravtsov et al. (2018), as the difference between $M_{\star,500c}$ and the BCG stellar mass, we see the same trend as for $M_{\star,500c}$. Finally, to consistently compare simulations with different resolutions, and to rule out that this overproduction of stars is caused by intracluster light (ICL) instead of being a problem of SHs, we compare total stellar masses of only well-resolved satellites (i.e., all sub-haloes with masses of $M_{SH} > 2 \times 10^{10} M_{\odot}$, as defined in Sect. 2.3). In the bottom panel of Fig. 1, we show that the B20 model produces the SHs with the highest stellar masses, followed by R15 and RF18. In addition, $10 \times B20$ has systematically higher stellar masses than $1 \times B20$, which shows that with increasing resolution there is an increase of high stellar mass SHs.

In Fig. 2, we show the average cumulative satellite SH mass number count (left column for total mass and right column for stellar mass) both within the virial radius (upper panels) and within a cluster-centric distance $R < 0.15R_{vir}$ (bottom panels) for the four regions (D3, D6, D18, and D25) presented in Table 2 that are in common between all suites. We also compare the theoretical estimates against the observed mass distributions derived by Granata et al. (2022) and Bergamini et al. (2019) for the cluster AS1063.

The total-mass count functions within R_{vir} (Fig. 2, top left panel) resemble a power law, in agreement with other theoretical studies (Giocoli et al. 2008). The $1 \times$ simulations deviate from the power-law behaviour at masses $\lesssim 2 \times 10^{10} h^{-1} M_{\odot}$, indicating that resolution limits become significant at these mass scales. This result validates our choice of excluding the SHs below the mass limit discussed in Sect. 2.2 from our analysis.

If we focus on the total-mass count within $0.15R_{vir}$ (lower panels), we find that different setups produce significantly different numbers of SHs, and setups with larger softening produce a too small number of SHs. This is probably due to the fact

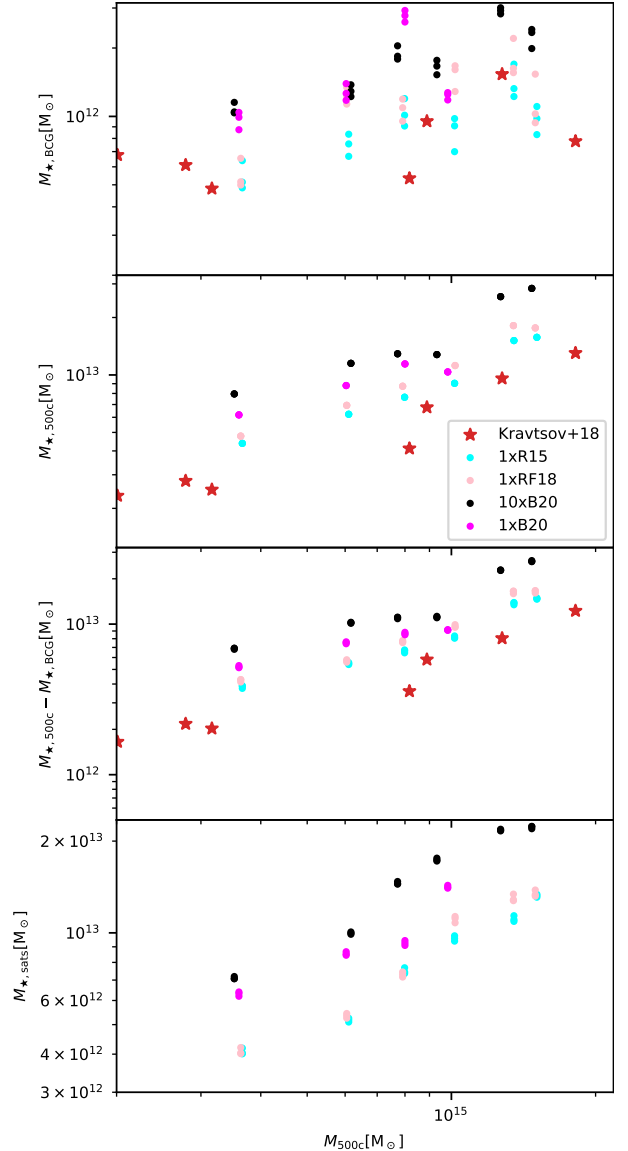


Fig. 1. Comparison of BCG mass (*first panel*), stellar mass (*second panel*), and satellite (i.e., stellar mass minus BCG mass, *third panel*) values and the stellar mass sum of all well-resolved SHs within R_{vir} (*fourth panel*) within R_{500c} for our four suites (circles coloured as in the label) and with the observational data from Kravtsov et al. (2018) (red stars). BCG masses are computed within a projected aperture of 50 physical kpc, and for each region we present masses from three orthogonal projections. *From left to right*, data points correspond to the main haloes of the following regions: D25, D3, D6, D18, D10, and D1 presented in Table 2.

that large-softening simulations produce more fragile SH cores, which are less resistant to tidal forces.

We further studied the over-production of stars by showing the cumulative number count of SHs with a given stellar mass. We present the cumulative number within R_{vir} in the top right panel of Fig. 2, where we see that $1 \times R15$ and $1 \times RF8$ produce SHs with very similar stellar masses (except a small difference at $M_{\star} \approx 3-4 \times 10^{10} M_{\odot}$), while $1 \times B20$ has many more bright galaxies (as expected by its lower feedback). $1 \times B20$ and $10 \times B20$ have nearly the same stellar mass counts. The stellar mass count inside $0.15R_{vir}$, (Fig. 2 bottom right panel) shows that a better resolution increases the number of high stellar mass galaxies.

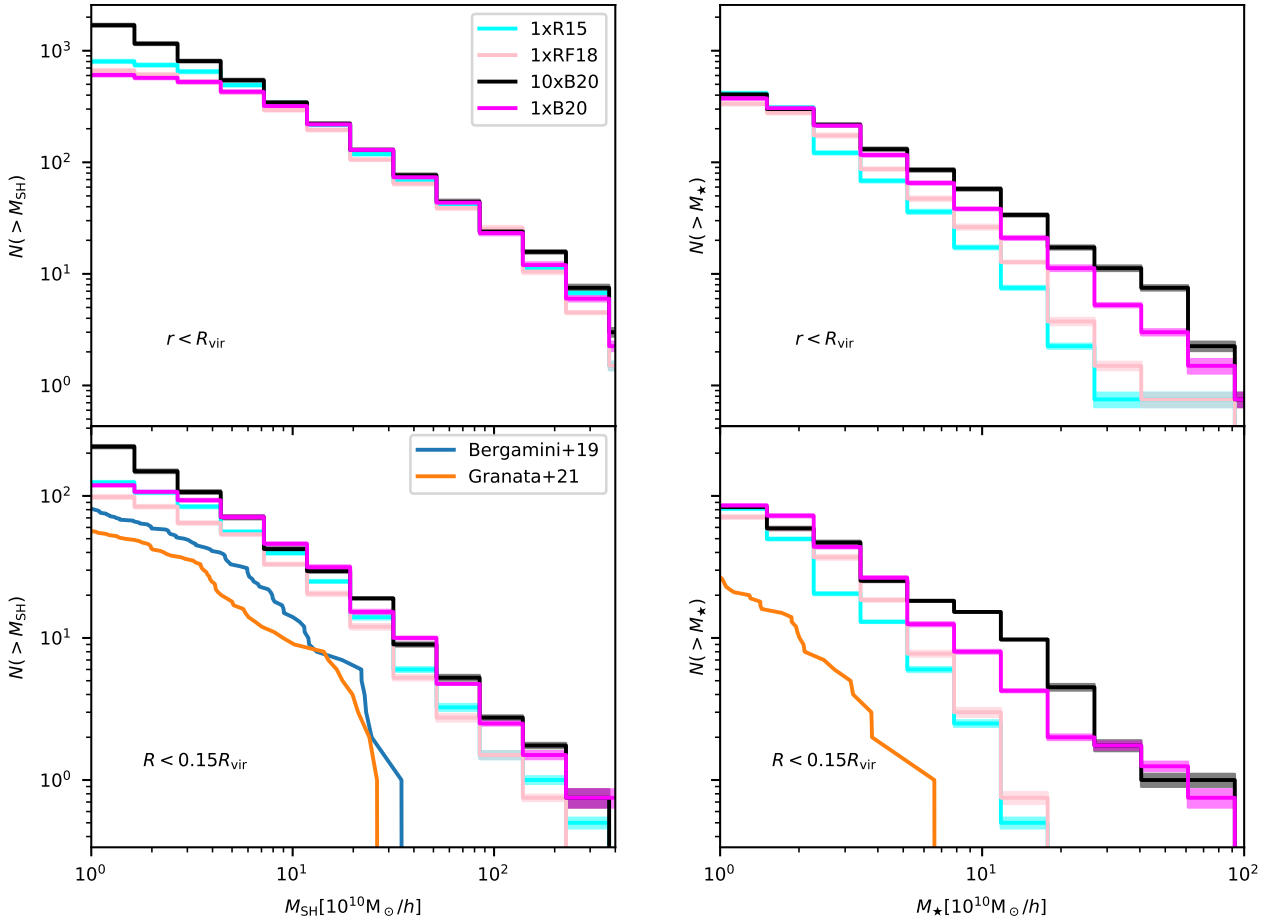


Fig. 2. Average cumulative number of satellite sub-structures with total mass larger than M_{SH} and lower than $10^{13} h^{-1} M_{\odot}$ (left column) and for stellar masses larger than M_{\star} , computed within an aperture of 30 physical kpc. We show data for the four $1 \times \text{R15}$ (cyan), $1 \times \text{RF18}$ (pink), $10 \times \text{B20}$ (black), and $1 \times \text{B20}$ (magenta) simulations in common between the four suites (i.e., D3, D6, D18, and D25 presented in Table 2). For each simulation we average data over three orthogonal projections. Shaded area represents standard deviation between different setups. *Upper panels* consider SHs within the virial radius and *lower panels* consider SHs with projected cluster-centric distance $R < 0.15R_{\text{vir}}$. *Left panels* show cumulative number of total SH mass M_{SH} , while *right panels* show cumulative mass of galaxy stellar mass associated with each SH. Observations are from the central region ($R < 0.15R_{\text{vir}}$) of cluster AS1063 presented in Bergamini et al. (2019) and Granata et al. (2022). Both simulations and observations have an average redshift of $z \approx 0.4$.

In particular, Granata et al. (2022) used a Salpeter (1955) IMF (see the appendix in Mercurio et al. 2021), whereas in our simulations we adopted a Chabrier (2003) IMF. We therefore re-scaled observational stellar masses by a factor of 0.58 to match values of a Chabrier IMF (as proposed in Speagle et al. 2014).

From the figure, we can evince that both feedback schemes and resolution parameters strongly affect the SH population in galaxy cluster cores, compared to their effect on the population within R_{vir} , especially when it comes to high-mass SHs ($M_{\text{SH}} > 4 \times 10^{11} h^{-1} M_{\odot}$); there are more massive SHs that reach the core of a galaxy cluster when increasing resolution or lowering feedback. We also note that $1 \times \text{RF18}$ and $1 \times \text{R15}$ simulations are the ones that best match observations of the galaxy mass distribution in the internal regions of galaxy clusters.

3.2. SH radial distributions

The impact of resolution and feedback on the total number of SHs in the central regions of clusters can be better appreciated in Fig. 3 (top panel), where we show the average number of SHs with a projected cluster-centric distance larger than a given fraction of the host virial radius. This is shown for the four regions

in common between our four setups, namely, D3, D6, D18, and D25 as in Table 2.

The average number of SHs in the central regions of clusters in the $1 \times \text{RF18}$ simulations is smaller than the corresponding number in the $1 \times \text{R15}$ simulations by $\sim 25\%$ (see Table 2). This behaviour is similar to what we found in Fig. 2 (bottom left), and is most probably caused by the relation between SH fragility in cluster cores and softening lengths.

From the bottom panel of Fig. 3, where we show the normalised distributions, we notice that simulations all have a very similar spatial concentration of SHs. If we compare the relative compactness with observations from Bergamini et al. (2019) (as already done in M20 for $1 \times \text{R15}$ simulations), we find that all suites are unable to reproduce the drop in the number count in the region $[0.07-0.1]R_{\text{vir}}$ that is found in observations.

3.3. Circular velocity vs. SH mass

In Fig. 4, we show the SH distribution in the $V_{\text{max}}-M_{\text{SH}}$ plane for all simulation suites, where V_{max} is computed as in Eq. (1). Each data point corresponds to a different SH. The SHs in the $10 \times \text{B20}$ and $1 \times \text{B20}$ simulations generally have higher

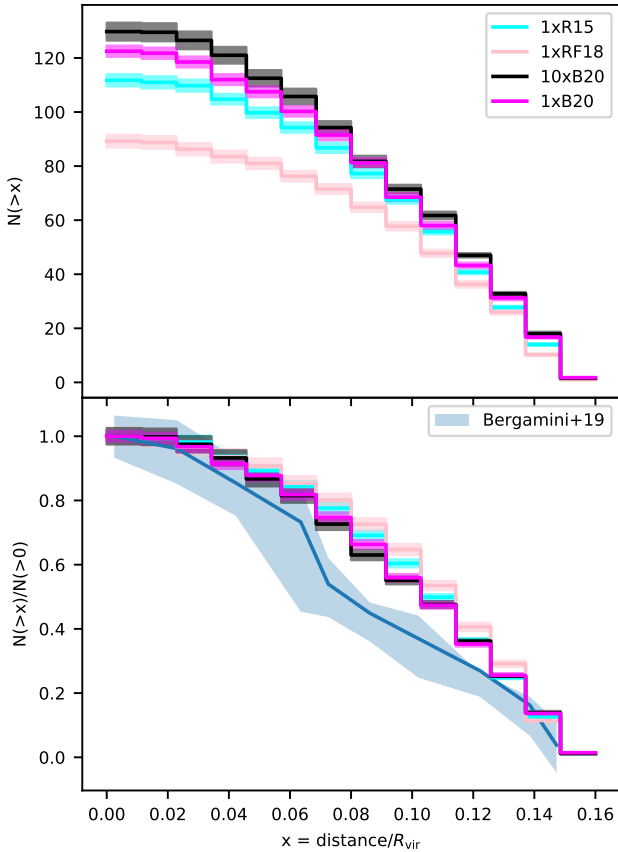


Fig. 3. Average cumulative number of SHs (*top panel*) and the same value normalised to unity (*bottom panel*) within a given projected cluster-centric distance in units of the host virial radius. Here, we only consider the four Dianoga regions in common between all four setups in Table 2, and SHs within a projected distance of $R < 0.15R_{\text{vir}}$ and a total mass greater than $2 \times 10^{10} h^{-1} M_{\odot}$. The black, cyan, and pink lines refer to the $10\times$, $1\times R15$, and $1\times RF18$ simulations, respectively. Shaded area shows data from Bergamini et al. (2019).

maximum circular velocities than in the $1\times R15$ and $1\times RF18$ simulations. The amount of this difference grows as a function of the SH mass. Consequently, the $V_{\text{max}}-M_{\text{SH}}$ relations in the $10\times B20$ and $1\times B20$ simulations are significantly steeper than the others.

For comparison, Fig. 4 shows the $V_{\text{max}}-M_{\text{SH}}$ relation of Bergamini et al. (2019) (blue solid lines) based on the strong lensing analysis of galaxy clusters MACS J1206.2–0847 ($z = 0.44$), MACS J0416.1–2403 ($z = 0.4$), and AbellS1063 ($z = 0.35$). M20 already showed that the SHs in the $1\times R15$ simulations fell below the observational relation of Bergamini et al. (2019) at all masses. Our results show that the same result holds for the $1\times RF18$ simulations. On the other hand, the gap between observations and simulations is reduced when the AGN feedback is less efficient (i.e., in the $10\times B20$ and $1\times B20$ simulations, although only for the SHs with the largest masses).

This behaviour is akin to that reported by Bahé (2021), who found that the SHs in the Hydrangea cluster simulations, implementing the Eagle galaxy formation model (Bahe et al. 2016), have V_{max} similar or even exceeding the Bergamini et al. (2019) relation at masses of $M_{\text{SH}} \gtrsim 10^{11} h^{-1} M_{\odot}$. Thus, we may interpret their results as an indication that in the sub-grid model implemented in Hydrangea SF is less efficient at a fixed halo mass.

At lower masses ($M_{\text{SH}} \approx 2 \times 10^{10} M_{\odot}$), the median SH maximum circular velocity in all our simulations reaches a

value of $\sim 100 \text{ km s}^{-1}$, almost independently of the resolution and feedback model. This value is very similar to the median value reported by Bahé (2021) in the same SH mass-range, and is it significantly below the observational relation of Bergamini et al. (2019). For example, at masses of $\sim 10^{10} h^{-1} M_{\odot}$, Bergamini et al. (2019) report an average V_{max} of $\sim 170 \text{ km s}^{-1}$. In a more recent work focused on AS1063 and implementing a different approach to model the contribution of the cluster galaxies to the cluster strong lensing signal, Granata et al. (2022) found that the typical maximum circular velocity of SHs in this mass range is $\sim 150 \text{ km s}^{-1}$.

We note that this same trend holds for the high-resolution simulations presented in Bahé (2021). Bahé (2021) reported the existence of a second branch of the $V_{\text{max}}-M_{\text{SH}}$ relation, followed by a minority of SHs with masses of $M_{\text{SH}} \lesssim 10^{11} h^{-1} M_{\odot}$, which is consistent with observations. Even in our simulations with the highest mass resolution, we do not find evidence for a bimodal $V_{\text{max}}-M_{\text{SH}}$ relation, although we notice that some SHs in the $10\times B20$ and $1\times B20$ simulations have V_{max} close to and even higher than the Bergamini et al. (2019) relation.

For the reasons outlined above and to provide a fair comparison with the data, in the next analyses we divided SHs in two samples; low-mass SHs with $M_{\text{SH}} \in [4, 6] \times 10^{10} h^{-1} M_{\odot}$, in order to have a large sample of both well-resolved SHs in a narrow mass range, and high-mass SHs with $M_{\text{SH}} \in [1, 6] \times 10^{11} h^{-1} M_{\odot}$, where the range is large enough to have a representative number of SHs in the high-mass regime. The low-mass SHs sample helped us study the mass-range observed in Bergamini et al. (2019), while the high-mass SHs sample helped us study the mass range where AGN feedback is most effective.

3.4. Mass and circular velocity profiles

3.4.1. Low-mass SHs

We turn our attention to the SH inner structure, which we quantify by means of the SH mass and circular velocity profiles. As shown in Fig. 5, the average difference between maximum circular velocities of SHs with masses of $5 \times 10^{10} h^{-1} M_{\odot} \leq M_{\text{SH}} \leq 10^{11} h^{-1} M_{\odot}$ in different simulations reduces to $\sim 15\%$, and it seems that simulations run with different feedback schemes (including the one used in the Hydrangea simulations, as shown in Fig. 4), resolution parameters, and softening lengths are unable to match the observed compactness.

3.4.2. High-mass SHs

The total SH circular velocity and mass profiles for all the four simulation suites are shown in Fig. 6, which refers to SHs with $M_{\text{SH}} > 10^{11} h^{-1} M_{\odot}$. We notice that several SHs have maximum circular velocities that exceed 300 km s^{-1} in both the $10\times B20$ and $1\times B20$ simulations. The mean maximum circular velocity of these SHs is $\sim 220 \text{ km s}^{-1}$. On average, the V_{max} of SHs with similar masses in the $1\times R15$ and $1\times RF18$ simulations are $\sim 20-30\%$ smaller.

The SH mass and circular velocity profiles have limited dependence on the mass resolution. On average, we cannot appreciate significant differences between the profiles of SHs in the $1\times B20$ and $10\times B20$ simulations.

The details of the DM and baryon mass distribution in the SHs have a significant dependence on the efficiency of the AGN energy feedback. The simulations with a less efficient feedback model (e.g., $10\times B20$ and $1\times B20$) cool more gas in the centre of their SHs. This process should lead to a more intense

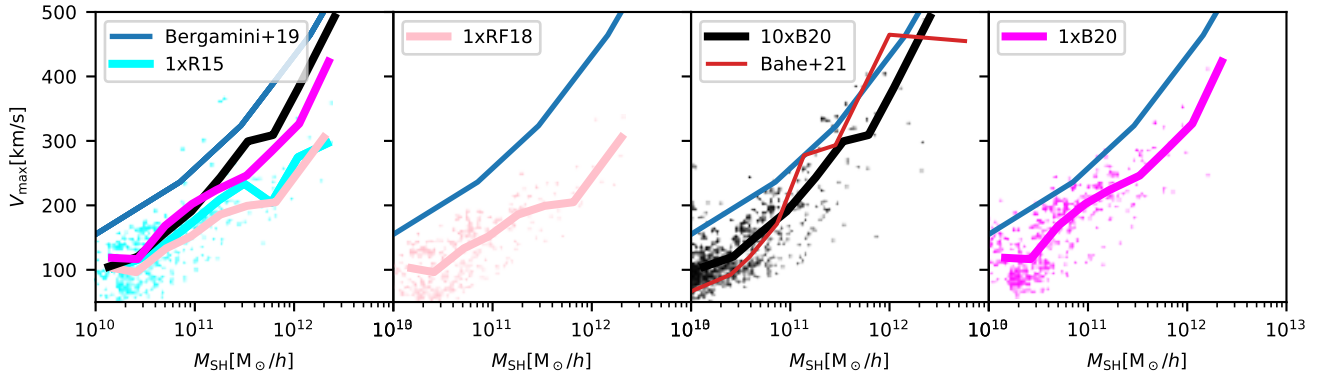


Fig. 4. V_{\max} vs. SH mass for $10 \times \text{B20}$ simulations (left panel), $1 \times \text{R15}$ (central panel), and $1 \times \text{RF18}$ (right panel), for all SHs (except for BCGs) with a projected distance ($R < 0.15R_{\text{vir}}$). The cyan, pink, black, and magenta lines refer to the $1 \times \text{R15}$, $1 \times \text{RF18}$, $10 \times \text{B20}$, and $1 \times \text{B20}$ simulations, respectively. The relation from Bergamini et al. (2019) is over-plotted in blue. We report data for $10 \times \text{B20}$ simulations (black solid line), a $1 \times \text{R15}$ simulation subset of $10 \times \text{B20}$ regions (solid cyan line), a $1 \times \text{RF18}$ simulation subset of $10 \times \text{B20}$ regions (pink line), and $1 \times \text{f}_{\text{SH}}$ (magenta line), for SHs with projected distances $< 0.15R_{\text{vir}}$ (right panel). We compare our high-resolution simulations with simulated data points of high-resolution Hydrangea simulations (Bahé et al. 2022) (red).

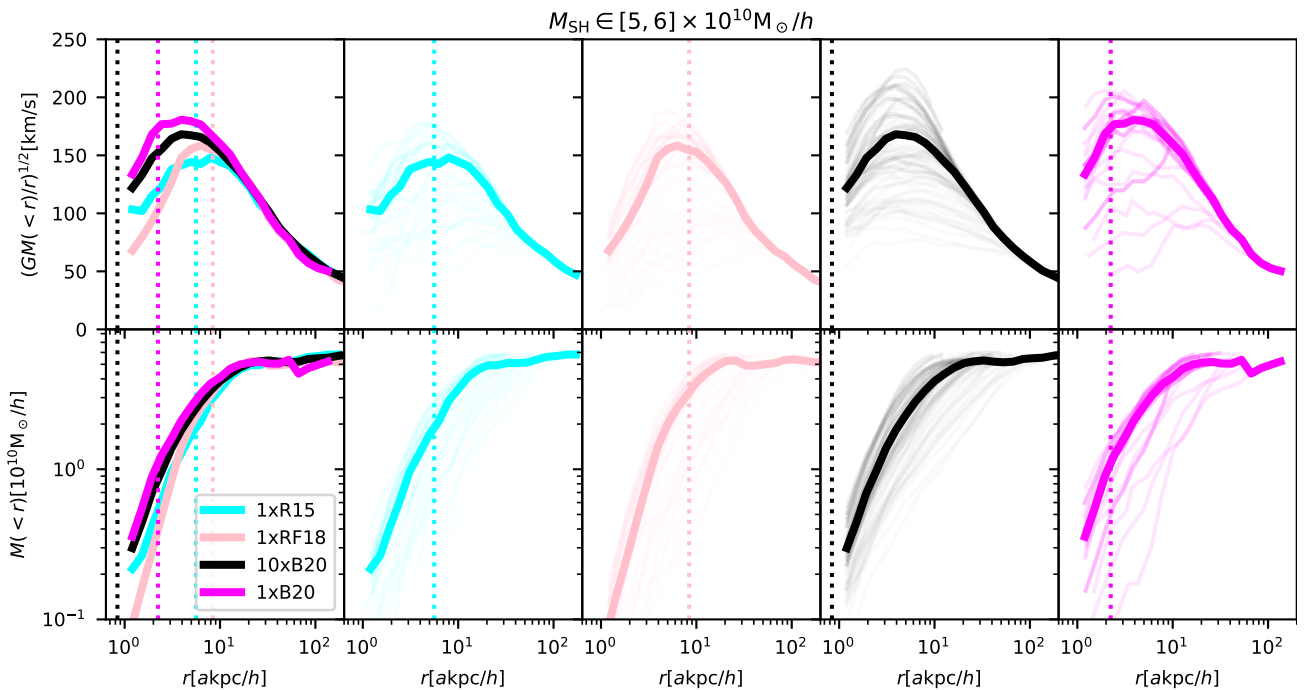


Fig. 5. Circular velocity profiles from total matter content of the SHs in the four cluster samples (upper row) and cumulative mass (lower row). The left most column shows the median values (thick solid lines) in radial bins for the $1 \times \text{R15}$, $1 \times \text{RF18}$, $10 \times$, and $1 \times \text{B20}$ simulations. The panels in other columns show profiles separately for each setup and single SHs (thin solid lines) together with their median values. SHs mass-range is $M_{\text{SH}} \in [5 \times 10^{10}, 6 \times 10^{10}] h^{-1} M_{\odot}$, with a projected distance smaller than $0.15R_{\text{vir}}$. For each setup, we plot the fiducial stellar resolution limit, $2.8\epsilon_*$, as vertical dashed lines.

star formation in these regions, and the creation of dense stellar cores. This effect is particularly evident in the SHs with large masses, as shown in the bottom panels of Fig. 7, where the average mass profiles and profiles of circular velocity of the DM and stars in SHs with masses of $M_{\text{SH}} > 10^{11} h^{-1} M_{\odot}$ are shown separately. In the $10 \times \text{B20}$ and $1 \times \text{B20}$ simulations, the stars dominate the total mass (i.e., sum of dark matter, gas, and star masses) profile within the inner $\lesssim 20\text{--}30 h^{-1}$ comoving kpc.

The high central stellar density in these simulations should also trigger the contraction of the dark matter haloes. Thus, the massive SHs in the $10 \times \text{B20}$ and $1 \times \text{B20}$ simulations are more compact and have higher maximum circular velocities compared to similar SHs in the $1 \times \text{R15}$ and $1 \times \text{RF18}$ samples. This

behaviour is clear in the upper panels of Fig. 7, showing the circular velocity profiles of DM and stars in the massive SHs separately. The $1 \times \text{R15}$ and $1 \times \text{RF18}$ simulations only differ significantly in the very inner regions of the SHs, because of their different softening scales.

3.5. Comparison with observations

A similar analysis of the mass and velocity profiles of lower mass SHs indicates that the impact of AGN feedback and the differences between the simulation types are mass dependent. In Fig. 8, we show the satellite SH central velocity dispersion σ (first panel, defined as $V_{\max}/\sqrt{2}$, as in Appendix C of

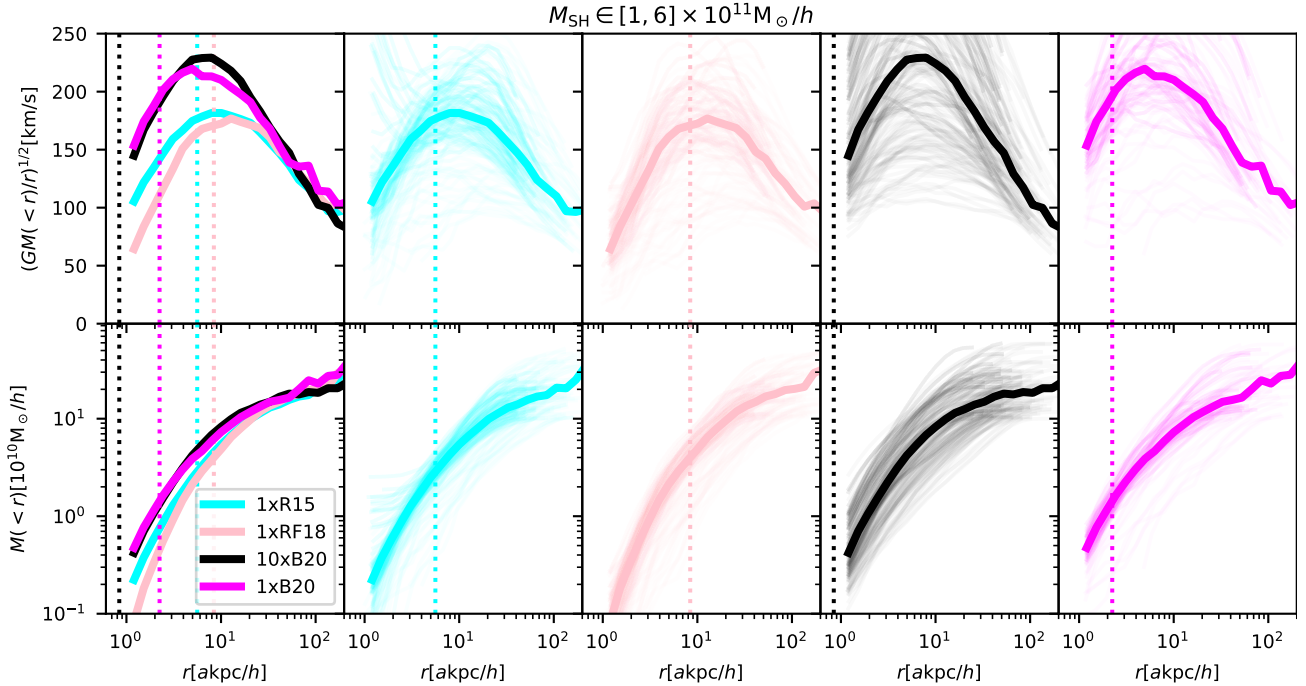


Fig. 6. Same as Fig. 5, but for SHs with masses of $M_{\text{SH}} \in [1 \times 10^{11}, 6 \times 10^{11}] h^{-1} M_{\odot}$.

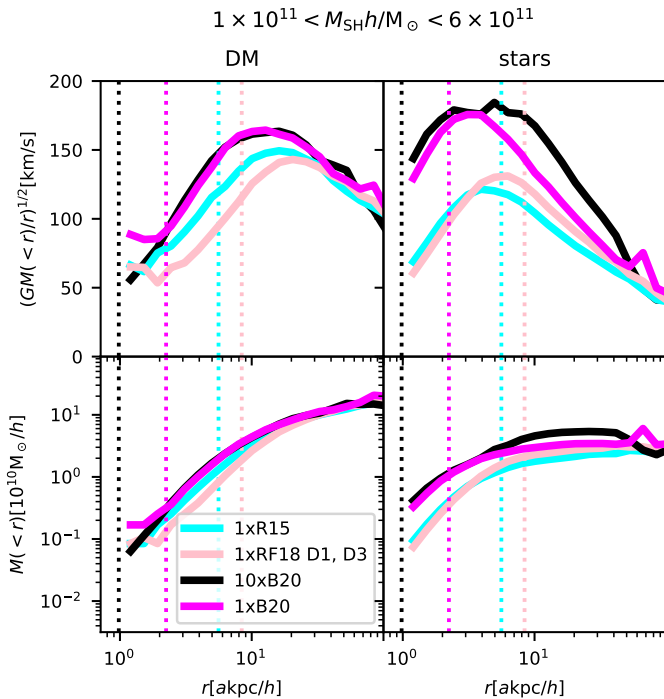


Fig. 7. Average profiles of circular velocity and cumulative mass per particle type: DM (left column), and stars (right column) for SHs with total masses in the range of $M_{\text{SH}} \in [1 \times 10^{11}, 6 \times 10^{11}] h^{-1} M_{\odot}$, for the four simulated suites coloured as in Fig. 4. For each setup we plot the corresponding $2.8\epsilon_{\star}$ (where ϵ_{\star} is the stellar softening) as vertical dashed lines. Overall order of line colours from top to bottom is, respectively, black, magenta, cyan, and pink.

Bergamini et al. 2019), the half mass radii (second and third panel, with $R_{50\%}$ for the total mass content and the projected stellar mass radius $R_{\star,50\%}$) and the stellar mass M_{\star} , (fourth panel) for SHs with velocity dispersion.

The first panel of Fig. 8 qualitatively shows the same results as Fig. 4. Here, Bergamini et al. (2019) used a fixed $\sigma-M_{\text{SH}}$ relation and determine the $\sigma-M_{\text{SH}}$ obtained using using a Faber–Jackson relation whose normalisation and slope are constrained by the observed kinematics of cluster members. Granata et al. (2022) had a fixed $R_{\star,50\%}-R_{\text{SH},50\%}$ relation and used a fundamental plane (FP) relation, calibrated using Hubble frontier fields photometry and data from the Multi Unit Spectroscopic Explorer on the Very Large Telescope. The FP relation was then adopted to compsorganiely fix the velocity dispersion of all members from their magnitudes and half-luminosity and radii. The second panel of Fig. 8 shows the half total mass radius of SHs. We see that simulations overestimate the SH sizes. These values are consistent with their compactness overestimation shown in the top panel of the same figure; in fact, the maximum circular velocity is a proxy for SH compactness (Bergamini et al. 2019). We see the same behaviour in the half stellar mass radius presented in the third panel of Fig. 8, where we show the half-mass radii of the stellar component vs. their SH mass. Here, we compare our data with results from Granata et al. (2022) using both their SH mass estimate (orange crosses) and the mass estimates from Bergamini et al. (2019) (green diamonds), and we see that simulations do underestimate stellar component compactness. In the fourth panel of Fig. 8, we compare the stellar mass against total mass of simulated SHs with observations, where we see that the stellar masses from low-mass simulated SHs ($M_{\text{SH}} < 10^{11} h^{-1} M_{\odot}$) do overlap the values from observations. We therefore conclude that low-mass simulated SHs have correct stellar fractions, but the level of compactness is too low (see first and second panels of the figure).

Concerning high-mass SHs ($M > 4 \times 10^{11}$ as in the fourth panel of Fig. 8), simulations do produce too many SHs. In fact, observations have no SHs in this mass regime.

We finally ruled out the possibility that such an increase of stellar mass is due to a wandering BH particle. In Fig. 9, we track the four most massive SHs of the D6 (10xB20) back in time and show that they had a nearest BH (searched within a

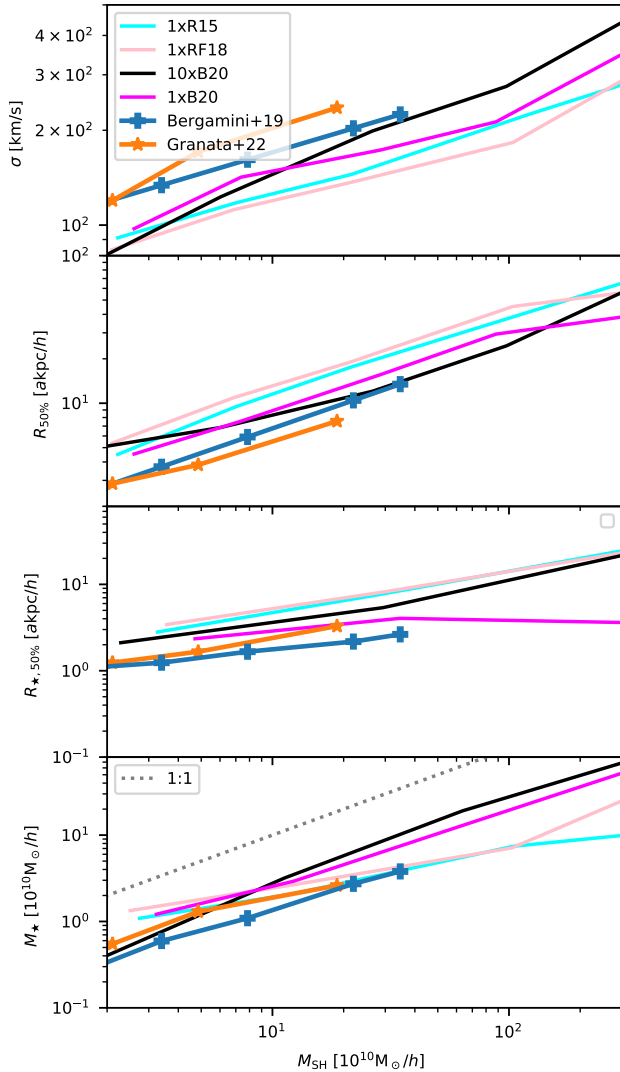


Fig. 8. Median velocity dispersion $\sigma = V_{\max}/\sqrt{2}$ (*top panel*), median half total mass radius $R_{50\%}$ (*second panel*), median half stellar mass projected radius $R_{*,50\%}$ (*third panel*), and median total stellar mass M_* (*fourth and last panels*), all vs. M_{SH} . In this plot, we exclude central SHs. Simulation suites are coloured as in Fig. 2. We also show median values of observations from cluster AS1063 presented in Bergamini et al. (2019) (blue solid lines with crosses) and Granata et al. (2022) (orange solid lines with diamonds). We also show Granata et al. (2022) radii (*third panel*) and stellar masses (*fourth panel*) over SH masses from Bergamini et al. (2019) via blue lines. Low-mass simulated SHs have stellar masses in agreement with observations, but they are too large, while high-mass simulated SHs are too numerous (no observations for SHs with $M_{\text{SH}} > 4 \times 10^{11} h^{-1} M_{\odot}$).

sphere of $20 \text{ akpc } h^{-1}$) and found that up to redshift $z \approx 0.3\text{--}0.4$, three of the four SHs have a BH near the centre (with distance $< 1 \text{ kpc}$), and all of them have a stellar mass that is growing smoothly.

Additionally, in Fig. 10 we show the $V_{\max}\text{--}M_{\text{SH}}$ relation and colour-code SH points by the distance of the nearest BH distance in units of the softening lengths (reported in Table 1). We notice that most of the massive haloes have a well-centred BH (i.e., within a gravitational softening radius), while low-massive ($M < 10^{11} h^{-1} M_{\odot}$) SHs tend to have no BHs. However, in this mass-range the SHs without BHs have probably not been seeded yet, and the V_{\max} parameter is under control.

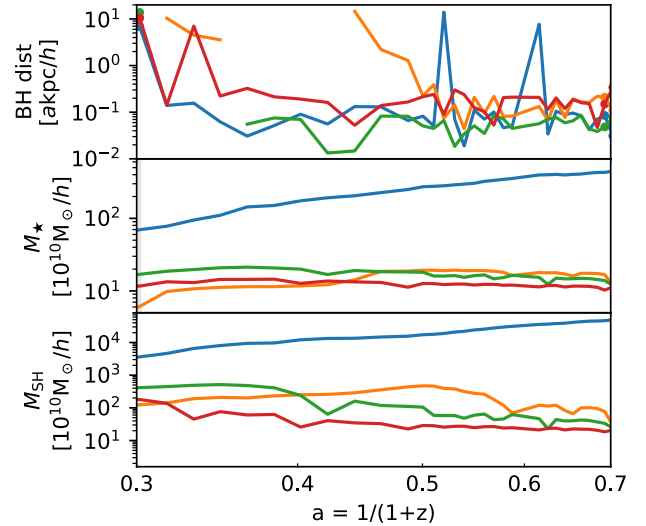


Fig. 9. Four most massive central SHs of D6 $10 \times \text{B20}$. *Upper panel* shows the distance from the nearest most massive black hole within $20 \text{ akpc } h^{-1}$, *central panel* shows the evolution of the stellar mass and *bottom panel* shows the evolution of the total SH mass. Each colour represents a different SH. The blue upper line is relative to the BCG.

4. Conclusions

We studied the discrepancy between observations and simulations found in M20 in detail, where it was found that observations show much more compact SHs than simulations. To this end, we analysed the properties of SHs in the cluster core of several hydrodynamic cosmological zoom-in simulations that were run with different resolutions, feedback schemes, and softening lengths.

In particular, we studied six Dianoga zoomed-in regions re-simulated with the fiducial model ($1 \times \text{R15}$) used in M20, a model with a larger softening and a different feedback scheme ($1 \times \text{RF18}$), and a model with higher resolution ($10 \times \text{B20}$) where feedback parameters have been re-calibrated to match observations at that resolution. We also ran their $1 \times$ counterpart, $1 \times \text{B20}$, with the same exact feedback scheme as $10 \times \text{B20}$ simulations in order to disentangle resolution effects from those related to different implementations of AGN feedback.

We summarise with the following conclusions.

- Varying resolution levels, softening lengths, and feedback schemes does not significantly impact the $V_{\max}\text{--}M_{\text{SH}}$ relation in the SH mass-range of interest for GGSL (i.e., low-mass SHs with $M_{\text{SH}} < 10^{11} h^{-1} M_{\odot}$), and all the simulations that we considered are unable to reproduce SH compactness as observed by Bergamini et al. (2019). These same results hold for Hydrangea simulations presented in Bahé (2021).
- Some setups ($1 \times \text{B20}$, $10 \times \text{B20}$, and Hydrangea simulations) are capable of producing a significant increase of V_{\max} in high-mass SHs ($M_{\text{SH}} > 4 \times 10^{11} h^{-1} M_{\odot}$), and they do match the observed $V_{\max}\text{--}M_{\text{SH}}$ scaling relation. However, this mass range is not of interest for GGSL comparisons, because observations find almost no SHs in this mass range.
- We found that simulations with a high number of massive SHs also have unrealistically high stellar masses due to a low-efficiency AGN feedback. The fact that some of the current simulations produce exceedingly high stellar masses was already found in works such as RF18 and B20, and most likely this very problem plagues the Hydrangea simulations

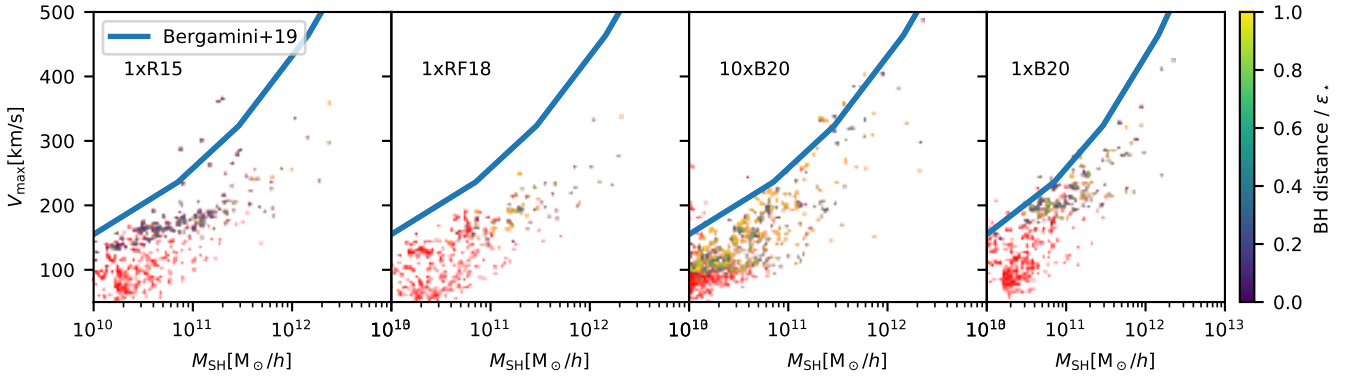


Fig. 10. Same as Fig. 4, where points are colour-coded (bar on the right) by the distance of the nearest BH from the SH centre, in units of the respective gravitational softening length reported in Table 1. Red points indicate SHs with no BH within 20 comoving kpc h^{-1} .

too, as shown in Fig. 1 in [Ragone-Figueroa et al. \(2018\)](#) and the right panel of Fig. 4 in [Bahé et al. \(2017\)](#).

- Given that different schemes produce different V_{\max} relations on high-mass SHs, we find partial agreement with [Robertson \(2021\)](#), in that current high-resolution simulations are not capable of constraining the Λ CDM paradigm. However, we find that this is only true for high-mass SHs ($M_{\text{SH}} > 4 \times 10^{11} h^{-1} M_{\odot}$) and that properties of low-mass SHs ($M_{\text{SH}} < 10^{10} h^{-1} M_{\odot}$) can be used in future simulations to constrain cosmology.

In this work, we found that the discrepancy between observations and simulations found in [M20](#) cannot be solved by simply calibrating the feedback efficiency of simulations, because this would lead to an unrealistically high number of bright galaxies. Thus, it seems that modern hydrodynamic simulations cannot reproduce both compactness and stellar masses of SHs in the internal regions of galaxy clusters.

Finally, we find that the $V_{\max}-M_{\text{SH}}$ at $M_{\text{SH}} \lesssim 10^{11} h^{-1} M_{\odot}$, which is the most relevant mass-range in GGSL, shows tension between observations and simulations of different resolutions and feedback parameters. [Meneghetti et al. \(2022\)](#) found that all our simulations have problems in recovering GGSL probability, in accordance with this work. In fact, while some simulations can produce an integrated GGSL in agreement with observations (as shown in their Fig. 3), it also true that the GGSL probability of these setups is dominated by the contribution of the largest secondary critical lines, as shown in their Fig. 7, where simulations overestimate the number density of large secondary critical lines.

The match between simulations and observed integrated GGSL found in [Robertson \(2021\)](#) is thus not surprising. It is likely due to an unrealistically high number of large secondary critical lines with respect to observations (as noted before, *Hydrangea* simulations do match the $V_{\max}-M_{\text{SH}}$ relation but only in the high-mass regime of SHs). This still challenges either the current feedback scheme or the underlying Λ CDM paradigm, or both.

Acknowledgements. We thank the anonymous referee for her/his comments that helped improve the presentation of our results. We acknowledge support from the grant PRIN-MIUR 2017 WSCC32. A.R. acknowledges support by MIUR-DAAD contract number 34843 “The Universe in a Box”. M.V. is supported by the Alexander von Humboldt Stiftung and the Carl Friedrich von Siemens Stiftung. M.V. and K.D. acknowledge support by the Deutsche Forschungsgemeinschaft (DFG, German Research Foundation) under Germany’s Excellence Strategy – EXC-2094 – 390783311. K.D. also acknowledges support through the COMPLEX project from the European Research Council (ERC) under the European Union’s Horizon 2020 research and inno-

vation program grant agreement ERC-2019-AdG 882679. We used Trieste IT framework ([Taffoni et al. 2020](#); [Bertocco et al. 2020](#)). We are especially grateful for the support by M. Petkova through the Computational centre for Particle and Astrophysics (C²PAP). P.N. acknowledges the Black Hole Initiative (BHI) at Harvard University, which is supported by grants from the Gordon and Betty Moore Foundation and the John Tempson Foundation, for hosting her. L.M. acknowledges the support from the grant ASI n.2018-23-HH.0.

References

- Bahé, Y. M. 2021, *MNRAS*, 505, 1458
 Bahe, Y. M., Crain, R. A., Kauffmann, G., et al. 2016, *MNRAS*, 456, 1115
 Bahé, Y. M., Barnes, D. J., Dalla Vecchia, C., et al. 2017, *MNRAS*, 470, 4186
 Bahé, Y. M., Schaye, J., Schaller, M., et al. 2022, *MNRAS*, 516, 167
 Bassini, L., Rasia, E., Borgani, S., et al. 2020, *A&A*, 642, A37
 Beck, A. M., Murante, G., Arth, A., et al. 2016, *MNRAS*, 455, 2110
 Bergamini, P., Rosati, P., Mercurio, A., et al. 2019, *A&A*, 631, A130
 Bernardi, M., Meert, A., Sheth, R. K., et al. 2013, *MNRAS*, 436, 697
 Bertocco, S., Goz, D., Tornatore, L., et al. 2020, in *ASP Conf. Ser.*, eds. R. Pizzo, E. R. Deul, J. D. Mol, J. de Plaa, & H. Verkouter, 527, 303
 Bhattacharyya, S., Adhikari, S., Banerjee, A., et al. 2022, *ApJ*, 932, 30
 Bonafede, A., Dolag, K., Stasyszyn, F., Murante, G., & Borgani, S. 2011, *MNRAS*, 418, 2234
 Borgani, S., Dolag, K., Murante, G., et al. 2006, *MNRAS*, 367, 1641
 Chabrier, G. 2003, *PASP*, 115, 763
 Davis, M., Efstathiou, G., Frenk, C. S., & White, S. D. M. 1985, *ApJ*, 292, 371
 Despali, G., & Vegetti, S. 2017, *MNRAS*, 469, 1997
 Despali, G., Giocoli, C., Angulo, R. E., et al. 2016, *MNRAS*, 456, 2486
 Despali, G., Lovell, M., Vegetti, S., Crain, R. A., & Oppenheimer, B. D. 2020, *MNRAS*, 491, 1295
 Dolag, K., Borgani, S., Murante, G., & Springel, V. 2009, *MNRAS*, 399, 497
 Eckert, D., Molendi, S., & Paltani, S. 2011, *A&A*, 526, A79
 Fabjan, D., Borgani, S., Tornatore, L., et al. 2010, *MNRAS*, 401, 1670
 Ferland, G. J., Korista, K. T., Verner, D. A., et al. 1998, *PASP*, 110, 761
 Gao, L., White, S. D. M., Jenkins, A., Stoehr, F., & Springel, V. 2004, *MNRAS*, 355, 819
 Genel, S., Vogelsberger, M., Springel, V., et al. 2014, *MNRAS*, 445, 175
 Giocoli, C., Tormen, G., & van den Bosch, F. C. 2008, *MNRAS*, 386, 2135
 Granata, G., Mercurio, A., Grillo, C., et al. 2022, *A&A*, 659, A24
 Green, S. B., van den Bosch, F. C., & Jiang, F. 2021, *MNRAS*, 503, 4075
 Grillo, C., Suyu, S. H., Rosati, P., et al. 2015, *ApJ*, 800, 38
 Hernquist, L. 1987, *ApJS*, 64, 715
 Hirschmann, M., Dolag, K., Saro, A., et al. 2014, *MNRAS*, 442, 2304
 Kneib, J.-P., & Natarajan, P. 2011, *A&ARv*, 19, 47
 Kravtsov, A. V., & Borgani, S. 2012, *ARA&A*, 50, 353
 Kravtsov, A. V., Vikhlinin, A. A., & Meshcheryakov, A. V. 2018, *Astron. Lett.*, 44, 8
 Lotz, J. M., Koekemoer, A., Coe, D., et al. 2017, *ApJ*, 837, 97
 Ludlow, A. D., Schaye, J., Schaller, M., & Bower, R. 2020, *MNRAS*, 493, 2926
 Magorrian, J., Tremaine, S., Richstone, D., et al. 1998, *AJ*, 115, 2285
 Meneghetti, M., Natarajan, P., Coe, D., et al. 2017, *MNRAS*, 472, 3177
 Meneghetti, M., Davoli, G., Bergamini, P., et al. 2020, *Science*, 369, 1347
 Meneghetti, M., Ragagnin, A., Borgani, S., et al. 2022, *A&A*, submitted [arXiv:2204.09065]
 Mercurio, A., Rosati, P., Biviano, A., et al. 2021, *A&A*, 656, A147

- Moore, B., Governato, F., Quinn, T., Stadel, J., & Lake, G. 1998, *ApJ*, **499**, L5
- Muldrew, S. I., Pearce, F. R., & Power, C. 2011, *MNRAS*, **410**, 2617
- Naderi, T., Malekjani, M., & Pace, F. 2015, *MNRAS*, **447**, 1873
- Natarajan, P., & Kneib, J.-P. 1997, *MNRAS*, **287**, 833
- Natarajan, P., & Springel, V. 2004, *ApJ*, **617**, L13
- Natarajan, P., De Lucia, G., & Springel, V. 2007, *MNRAS*, **376**, 180
- Natarajan, P., Ricarte, A., Baldassare, V., et al. 2019, *Bull. Am. Astron. Soc.*, **51**, 73
- Nguyen, Q. L., Mathews, G. J., Phillips, L. A., et al. 2021, *Mod. Phys. Lett. A*, **36**, 2130001
- Planelles, S., Fabjan, D., Borgani, S., et al. 2017, *MNRAS*, **467**, 3827
- Postman, M., Coe, D., Benítez, N., et al. 2012, *ApJS*, **199**, 25
- Ragagnin, A., Fumagalli, A., Castro, T., et al. 2021, *A&A*, submitted [arXiv:2110.05498]
- Ragone-Figueroa, C., Granato, G. L., Murante, G., Borgani, S., & Cui, W. 2013, *MNRAS*, **436**, 1750
- Ragone-Figueroa, C., Granato, G. L., Ferraro, M. E., et al. 2018, *MNRAS*, **479**, 1125
- Ragone-Figueroa, C., Granato, G. L., Borgani, S., et al. 2020, *MNRAS*, **495**, 2436
- Rasia, E., Borgani, S., Murante, G., et al. 2015, *ApJ*, **813**, L17
- Robertson, A. 2021, *MNRAS*, **504**, L7
- Salpeter, E. E. 1955, *ApJ*, **121**, 161
- Schaye, J., Craun, R. A., Bower, R. G., et al. 2015, *MNRAS*, **446**, 521
- Shakura, N. I., & Sunyaev, R. A. 1973, *A&A*, **24**, 337
- Speagle, J. S., Steinhardt, C. L., Capak, P. L., & Silverman, J. D. 2014, *ApJS*, **214**, 15
- Springel, V. 2005, *MNRAS*, **364**, 1105
- Springel, V., White, S. D. M., Tormen, G., & Kauffmann, G. 2001, *MNRAS*, **328**, 726
- Springel, V., Di Matteo, T., & Hernquist, L. 2005a, *MNRAS*, **361**, 776
- Springel, V., White, S. D. M., Jenkins, A., et al. 2005b, *Nature*, **435**, 629
- Steinborn, L. K., Dolag, K., Hirschmann, M., Prieto, M. A., & Remus, R.-S. 2015, *MNRAS*, **448**, 1504
- Taffoni, G., Becciani, U., Garilli, B., et al. 2020, in *ASP Conf. Ser.*, eds. R. Pizzo, E. R. Deul, J. D. Mol, J. de Plaa, & H. Verkouter, 527, 307
- Taylor, P., & Kobayashi, C. 2015, *MNRAS*, **448**, 1835
- Tormen, G., Diaferio, A., & Syer, D. 1998, *MNRAS*, **299**, 728
- Tornatore, L., Borgani, S., Dolag, K., & Matteucci, F. 2007, *MNRAS*, **382**, 382
- Tremmel, M., Quinn, T. R., Ricarte, A., et al. 2019, *MNRAS*, **483**, 3336
- Umetsu, K. 2020, *A&ARv*, **28**, 7
- van den Bosch, F. C., Yang, X., Mo, H. J., & Norberg, P. 2005, *MNRAS*, **356**, 1233
- Wurster, J., & Thacker, R. J. 2013, *MNRAS*, **431**, 2513
- Yang, D., & Yu, H.-B. 2021, *Phys. Rev. D*, **104**, 103031
- Zitrin, A., Fabris, A., Merten, J., et al. 2015, *ApJ*, **801**, 44
-
- ¹ Dipartimento di Fisica e Astronomia “Augusto Righi”, Alma Mater Studiorum Università di Bologna, Via Gobetti 93/2, 40129 Bologna, Italy
e-mail: antonio.ragagnin@unibo.it
- ² INAF – Osservatorio Astronomico di Trieste, Via G.B. Tiepolo 11, 34143 Trieste, Italy
- ³ IFPU – Institute for Fundamental Physics of the Universe, Via Beirut 2, 34014 Trieste, Italy
- ⁴ INAF-Osservatorio di Astrofisica e Scienza dello Spazio di Bologna, Via Piero Gobetti 93/3, 40129 Bologna, Italy
- ⁵ INFN-Sezione di Bologna, Viale Berti Pichat 6/2, 40127 Bologna, Italy
- ⁶ Centre for Theoretical Astrophysics and Cosmology, Institute for Computational Science, University of Zurich, Winterthurerstrasse 190, 8057 Zürich, Switzerland
- ⁷ Instituto de Astronomía Teórica y Experimental (IATE), Consejo Nacional de Investigaciones Científicas y Técnicas de la República Argentina (CONICET), Universidad Nacional de Córdoba, Laprida 854, X5000BGR Córdoba, Argentina
- ⁸ Zentrum für Astronomie der Universität Heidelberg, Institut für Theoretische Astrophysik, Albert-Ueberle-Str. 2, 69120 Heidelberg, Germany
- ⁹ Dipartimento di Fisica, Università degli Studi di Milano, Via Celoria 16, 20133 Milano, Italy
- ¹⁰ Universitäts-Sternwarte, Fakultät für Physik, Ludwig-Maximilians-Universität München, Scheinerstr.1, 81679 München, Germany
- ¹¹ Astronomy Unit, Department of Physics, University of Trieste, Via Tiepolo 11, 34131 Trieste, Italy
- ¹² Max-Planck-Institut für Astrophysik (MPA), Karl-Schwarzschild Strasse 1, 85748 Garching bei München, Germany
- ¹³ INAF – IASF Milano, Via A. Corti 12, 20133 Milano, Italy
- ¹⁴ INAF-Osservatorio Astronomico di Capodimonte, Via Moiariello 16, 80131 Napoli, Italy
- ¹⁵ Department of Astronomy, Yale University, New Haven, CT, USA
- ¹⁶ Dipartimento di Fisica e Scienze della Terra, Università degli Studi di Ferrara, Via Saragat 1, 44122 Ferrara, Italy, Zürich, Switzerland